Title

Greenhouse- and orbital-forced climate extremes during the early Eocene

Journal

Philosophical Transactions of the Royal Society A Mathematical Physical and Engineering Sciences, 376(2130)

ISSN

1364-503X

Authors

Kiehl, Jeffrey T
Shields, Christine A
Snyder, Mark A
et al.

Publication Date

2018-10-13

DOI

10.1098/rsta.2017.0085

Peer reviewed

PHILOSOPHICAL TRANSACTIONS A

rsta.royalsocietypublishing.org

Research

Cite this article: Kiehl JT, Shields CA, Snyder MA, Zachos JC, Rothstein M. 2018 Greenhouse- and orbital-forced climate extremes during the early Eocene. *Phil. Trans. R. Soc. A* **376**: 20170085.
http://dx.doi.org/10.1098/rsta.2017.0085

Accepted: 27 April 2018

One contribution of 11 to a discussion meeting issue 'Hyperthermals: rapid and extreme global warming in our geological past'.

Subject Areas:
palaeontology

Keywords:
climate change, Palaeocene–Eocene Thermal Maximum, hydrological cycle

Author for correspondence:
Jeffrey T. Kiehl
e-mail: jkiehl@ucsc.edu

Electronic supplementary material is available online at https://dx.doi.org/10.6084/m9.figshare.c.4205174.

THE ROYAL SOCIETY PUBLISHING

Greenhouse- and orbital-forced climate extremes during the early Eocene

Jeffrey T. Kiehl[1], Christine A. Shields[2], Mark A. Snyder[1], James C. Zachos[1] and Mathew Rothstein[1]

[1]University of California, Santa Cruz, 1156 High Street, Santa Cruz, CA 95064, USA
[2]National Center for Atmospheric Research, PO Box 3000, Boulder, CO 80307, USA

JTK, 0000-0001-5812-6552

The Palaeocene–Eocene Thermal Maximum (PETM) was a significant global warming event in Earth's deep past (56 Mya). The warming across the PETM boundary was driven by a rapid rise in greenhouse gases. The event also coincided with a time of maximum insolation in Northern Hemisphere summer. There is increased evidence that the mean warming was accompanied by enhanced seasonality and/or extremes in precipitation (and flooding) and drought. A high horizontal resolution (50 km) global climate model is used to explore changes in the seasonal cycle of surface temperature, precipitation, evaporation minus precipitation and river run-off for regions where proxy data are available. Comparison for the regions indicates the model accurately simulates the observed changes in these climatic characteristics with North American interior warming and drying, and warming and increased river run-off at other regions. The addition of maximum insolation in Northern Hemisphere summer leads to a drier North America, but wetter conditions at most other locations. Long-range transport of atmospheric moisture plays a critical role in explaining regional changes in the water cycle. Such high-frequency variations in precipitation might also help explain discrepancies or misinterpretation of some climate proxies from the

same locations, especially where sampling is coarse, i.e. at or greater than the frequency of precession.

This article is part of a discussion meeting issue 'Hyperthermals: rapid and extreme global warming in our geological past'.

1. Introduction

Earth's climate is currently experiencing dramatic changes as greenhouse gas levels rapidly rise due to the burning of fossil fuels. If humans continue to rely on these fuels as the major source of energy, then levels of atmospheric carbon dioxide are projected to more than triple pre-industrial levels. Such levels of atmospheric CO_2 have not existed on Earth for tens of millions of years. Given that climate models are used to study future scenarios of elevated CO_2, it is imperative to use the same climate models to explore how accurately they reproduce climates of the deep past. Thus, palaeoclimate modelling provides a unique and necessary test for models being used to project future climate change under elevated greenhouse gas concentrations.

The early Eocene hyperthermals represent extreme warm intervals suitable for exploring with climate models. This is especially true for the onset of the largest hypothermal, the Palaeocene–Eocene Thermal Maximum (PETM), given the extensive database for this event. Palaeo-proxy data show clear evidence for a large release of greenhouse gases over a geologically short time period at the onset of the PETM. The data indicate clear evidence for a global warming of approximately 5°C [1–5]. Data also provide information on the response of Earth's hydrological cycle to planetary warming [6–13]. Changes in greenhouse gases were not the only forcing agents influencing the PETM. Orbital variations due to the gravitational effects on Earth by the Sun and outer planets led to variations in the seasonal and latitudinal distribution of solar irradiance at the top of Earth's atmosphere. Note that changes in eccentricity (the elliptical shape of Earth's orbit about the Sun), one of the three orbital variations, regulate the total amount of solar energy reaching Earth, but the total energy input varies little due to changes in eccentricity. Studies [14–19] indicate that at the onset of the PETM Earth was experiencing near-maximum solar irradiance due to variations in eccentricity. It is important to understand the way these orbital changes to the distribution of solar irradiance contributed to climate change at the onset of the PETM. To our knowledge, there is only one study that explores the role of orbital forcing in changes in terrestrial climate during the PETM [20]. Other orbital forcing model studies have focused on ocean processes [21], or explored a large parameter space to determine dominant orbital and greenhouse factors contributing to PETM [22], while additional modelling studies have focused on the role of orbital forcing in carbon release during the Eocene [23,24]. The current orbital studies focus primarily on responses of the terrestrial seasonal cycle to changes in orbital forcing, similar to [20], and, as such, we will when possible compare our results with the findings in [20].

As the climate warms, not only does the mean climate state shift, but also the likelihood of extremes changes. Interest has increased in how extremes in temperature and other climate variables will change with future warming of the planet. Studies indicate (e.g. [25,26]) that significant shifts are occurring and will continue to occur in the future with regard to increased heat waves, extreme weather events and tropical storms. Given that extremes can play a significant role in defining boundaries for physical and biological systems, we also explore how extremes in Earth's water cycle changed at the onset of the PETM.

The study is organized as follows: §2 provides scientific motivation for the current research, §3 describes the models used in the study and the overall methodology, §4 presents the major results from the various climate model simulations. Model results are compared with palaeo-proxy data when possible. Finally, §5 presents the conclusion from this work.

2. Motivation

The motivations for this study are fourfold: (i) to explore the sensitivity of Earth's climate system to greenhouse gas forcing versus orbital forcing; (ii) to compare simulated changes in the seasonal hydrological cycle with palaeo-proxy data for specific geographical sites; (iii) to explore how the frequency of extreme events changes under various forcings; and (iv) to compare climatic changes that occurred at the PETM with changes expected to occur at the end of the twenty-first century under elevated greenhouse forcing. Regarding the first motivation, it is important to recognize that we are not carrying out transient simulations across the PETM event, but simulating time slices under various forcings to compare and contrast how the climate system responds to these forcings. With regard to the second motivation, given our time slice approach, we cannot look at specific timings of changes, but are looking for general characteristics between model simulations and proxy results. With regard to the fourth motivation, we do not argue that the PETM is a direct analogue for future climate change. What we wish to explore are how temperature and the water cycle respond under enhanced greenhouse forcing in terms of physical processes. For instance, to what extent do hydrological cycle processes respond in a similar manner for past and future greenhouse-forced climates?

A growing body of observational data indicate that extremes in hydrological climatic variables were higher for the PETM (e.g. [6–10]). In particular, Carmichael *et al*. [13] review various palaeo-proxy methods used to study past changes in hydrological variables and conclude that, during the PETM, 'There is … strong evidence in many regions for changes in the episodic and/or intra-annual distribution of precipitation…'. It is therefore important to see if climate models can reproduce these observed shifts in higher-frequency statistics. Proxies for precipitation and river run-off both indicate significant changes in hydrological variables on local or regional scales. Modelling regional changes in the hydrological cycle presents a real challenge to climate models that have traditionally been run at coarse horizontal resolutions of a few hundred kilometres. Studies [27–29] for present-day conditions convincingly find that resolutions of 100 km or more are incapable of representing important aspects of regional water cycles. The conclusion of these studies is that resolutions of 50 km or finer are required to carry out adequate analysis of regional water cycles. Presently, global climate models are carrying out simulations at 50 or 25 km resolution. Variable mesh global models are using even finer mesh sizes (approx. 5–10 km). So, we are now entering a stage in climate modelling in which climate and weather merge. It is in this spirit that the present study employs a high-resolution (50 km) global atmospheric model to study the deep time weather phenomena.

There is an additional advantage of using high spatial resolution for deep time climate simulations. Most proxy data reflect local conditions in the rocks and fossils of a particular core, outcrop or local field area. To make the strongest comparison, the fine geographical scale of the proxy data should be matched by model output at high spatial resolution. Thus, the present study is motivated to use a high-resolution model to more accurately simulate the local water seasonal cycle and to improve model–data comparisons.

3. Methodology

Using the community climate system model (CCSM) framework, a state-of-the-art Earth system model, we employ the high horizontal resolution ($0.47^\circ \times 0.63^\circ$) active atmosphere and land model components [30,31]. Community Atmosphere Model, v. 4 (CAM4), has 26 levels in the vertical and uses a finite volume dynamical core [32,33]. We will henceforth refer to this resolution as the 'half-degree' resolution.

In this study, we consider two different types of climate forcing, greenhouse gases and orbital parameters, for which all simulations assume the same fixed palaeogeography. In total, we present four simulations: (i) PETM (high) greenhouse gas values (table 1) with a modern orbital configuration; (ii) the PRE-PETM (low) greenhouse gas values with a modern orbital configuration (table 1); and (iii and iv) PETM greenhouse gas values with

Table 1. Boundary and climate forcing data for PRE-PETM, PETM, PETM-ORBMAX and PETM-ORBMIN half-degree CAM4 simulations. SST forcing was generated by the low-resolution fully coupled CCSM3. S_0 is the solar constant.

	PRE-PETM	PETM	PETM-ORBMAX	PETM-ORBMIN
CO_2 (ppmv)	1375	2250	2250	2250
CH_4 (ppmv)	0.76	16	16	16
obliquity (°)	23.5	23.5	24.5	22
eccentricity	0	0	0.06	0.06
vernal equinox (°)	0	0	270	90
S_0 (W m^{-2})	1355	1355	1355	1355
SST	PRE-PETM low-resolution CCSM3	PETM low-resolution CCSM3	PETM-ORBMAX low-resolution CCSM3	PETM-ORBMIN low-resolution CCSM3
geography	KS2013	KS2013	KS2013	KS2013
references in text	PETM boundary	greenhouse gas forcing only	greenhouse gas forcing + orbital forcing (maximum)	greenhouse gas forcing + orbital forcing (minimum)

an orbital configuration designed to provide the Northern Hemisphere summer with both maximum (ORBMAX) and minimum (ORBMIN) amounts of solar insolation (table 1 for orbital values).

Boundary forcing includes geography and land biomes, as well as sea surface temperature (SST) data. SSTs are generated by integrating the fully coupled, low-resolution version of the CCSM. The low-resolution CCSM3 experiments consist of active atmosphere, land, ocean and ice components with the atmosphere and land resolved on a T31 grid (3.75° × 3.75°) and nominal approximately 3° grid for the ocean and ice components [34]. Further details on the low-resolution PETM and PRE-PETM simulations can be found in Kiehl & Shields [35]. All simulations presented in this study employ the change to cloud drop properties described in [35].

The low-resolution CCSM3 SSTs simulated from the fully coupled simulations were then interpolated onto the half-degree grid of the CAM4; then the atmosphere simulations were carried out for a minimum of 20 years' duration. The lengths of these higher-resolution simulations were dictated by limited computational resources.

The dominant orbital configuration contributing to maximum seasonal warming/cooling is due to orbital precession. Following [20], we have chosen a configuration in this orbital variable to maximize/minimize Northern Hemisphere seasonal insolation. Figure 1*a*,*b* shows the change in the zonal mean solar insolation for the orbital configuration that maximizes summer insolation, and minimizes summer insolation, respectively. Figure 1*c* shows the difference between these two forcing scenarios. Note that orbital forcing variations impose enhanced seasonality at all latitudes. The orbital maximum and minimum PETM simulations will be referred to as 'ORBMAX' and 'ORBMIN', respectively. As noted, SSTs for all four CAM4 half-degree simulations were generated from four distinct low-resolution CCSM3 experiments, i.e. PETM-ORBMAX CAM4 simulation is forced by the CCSM3 PETM-ORBMAX low-resolution coupled climate simulation, etc. The CCSM3 coupled PETM experiments were spun up using a series of simulations totalling over 3000 years of coupled integration. The coupled simulations were preceded by 8000 year ocean-only simulations. The ocean-only runs were initialized with a best guess estimation of the PETM oceanic state and were then nudged with proxy data records using data assimilation techniques. This approach was used to accelerate the fully coupled

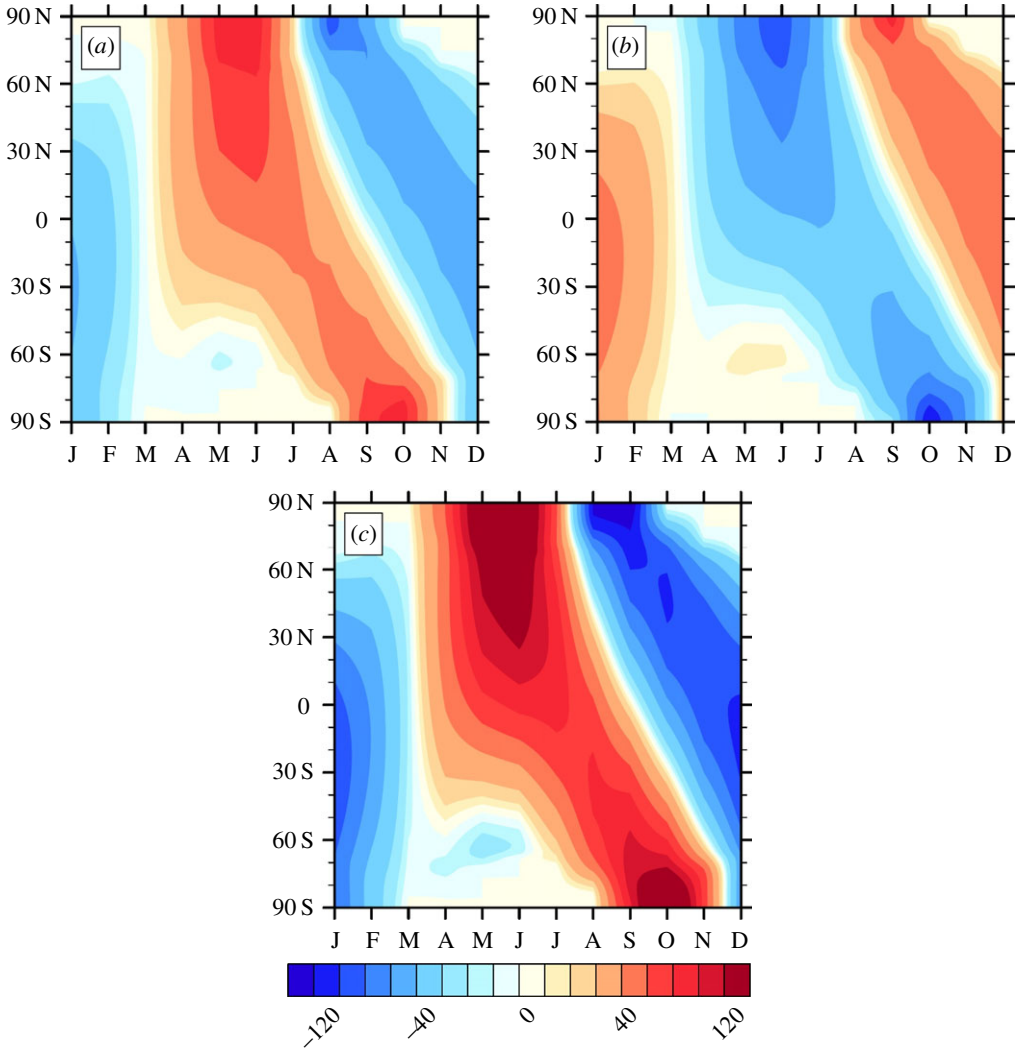

Figure 1. Change in the zonal mean top of atmosphere solar insolation (Wm^{-2}) for (*a*) maximum Northern Hemisphere summer orbital configuration minus control, (*b*) minimum Northern Hemisphere summer insolation minus control and (*c*) maximum minus minimum Northern Hemisphere summer insolation (table 1). Note that these orbital forcings have not been corrected for the calendar effect as in, for example, [36].

system, including the deep ocean, to an equilibrium state. SST forcing for the CCSM3 PETM coupled orbital simulations was initialized off the non-nudged PETM coupled simulation at year 800 after global mean sea surface trends were negligible. Each of the CCSM3 coupled simulations, ORBMAX and ORBMIN, was integrated for over 200 years to ensure surface equilibrium. Table 1 summarizes model experiments, greenhouse gas, orbital forcing, SST and boundary forcing data.

Regarding model data analysed for this study, regional hydroclimate is impacted by the weather and climate phenomena that occur with relatively high temporal frequency. In addition to including annual and seasonal time scales, we also present temperature and precipitation with daily frequencies more typical of extremes. Atmospheric river (AR) data are analysed using 6 hourly integrated water vapour and 850 mb winds. The detection algorithm used to identify AR data is a modified version of that described in [37,38].

4. Model results

(a) Global response

(i) Orbital signals only

Before contrasting the effects of greenhouse and orbital forcing across the PETM boundary, it is important to assess orbital forcing alone. A comparison between a PETM simulation that uses the control orbital configuration with a PETM simulation that employs the maximum orbital parameters is shown in figure 2, which includes annual differences (ORBMAX-PETM) for surface air temperature, precipitation, evaporation minus precipitation and soil moisture. The change in solar insolation between these two simulations is shown in figure 1*a*. The maximum orbital simulation enhances PETM warming of the high latitudes in the Northern Hemisphere (figure 2*a*), which is mainly due to greater forcing and more extensive land mass in the Northern Hemisphere. Cooling in the subtropical regions of modern-day China and Africa results from a decrease in solar forcing from September through March at these latitudes (figure 1*a*). The response of precipitation (figure 2*b*) to the change in orbital forcing shows enhanced monsoonal activity off western China and a latitudinal shift in the Inter-Tropical Convergence Zone. The simulated shifts in temperature in Africa and China are similar to those produced from simulations of the Last Interglacial or mid-Holocene, which are attributed to a change in land–ocean heating and effects on moisture advection from the ocean regions to land (e.g. [39]). As our applied changes in orbital forcing are similar to [39], the PETM results are most probably due to a similar mechanism. There is an overall decrease in North American rainfall due to two factors: (i) with maximum orbital forcing the Pacific subtropical high weakens, the subtropical jet shifts equatorwards, and there is moisture advection onto the North America continent; (ii) higher land temperatures lead to more severe surface drying over the mid-continental region. Simulated changes in evaporation minus precipitation (figure 2*c*) and upper layer soil moisture (figure 2*d*) indicate that increased orbital forcing leads to a drier interior in North America and a wetter interior of the Asian continent. These two responses result from the atmospheric dynamical changes described above. The significant increase in soil moisture in eastern China is due to enhanced filamentary atmospheric transport of moisture from the proto-Indian ocean, i.e. an atmospheric river. The largest forcing due to orbital variations is obtained by differencing simulations that employ minimum to maximum orbital parameters (figure 1*c* and table 1).

A comparison between a PETM simulation that uses the maximum orbital configuration and a PETM simulation that employs the minimum orbital parameters is shown in figure 3, which includes annual differences (ORBMAX-ORBMIN) for surface air temperature, precipitation, evaporation minus precipitation and soil moisture. The geographical changes in these climate variables are similar in geographical distribution to the results shown in figure 2, but with magnified amplitude. For example, changes in evaporation minus precipitation (figure 3*c*) exhibit excessive drying over North America, while eastern Asia is much wetter than that shown in figure 2*c*. Essentially, the larger change in solar insolation at high and mid-northern latitudes enhances the dynamical shift in atmospheric circulation patterns.

Comparison of our results with those in fig. 3 in [20] indicates good agreement in both magnitude and spatial pattern. For example, Lawrence *et al*. [20] simulate 6°C warming in the Arctic, which is similar to our simulation. They also show cooling in southern China and northern South America, which is very similar to our pattern of cooling. The major difference between our results and theirs is in the central region of the USA, where we simulate stronger warming.

(ii) Combined signals

We now consider the effects of greenhouse and orbital forcing in contributing to climate change at the onset of the PETM. A pair of simulations is used to elucidate the added effect of maximum orbital forcing occurring at the PETM. The first simulation assumes changes in greenhouse gas concentrations across the event (table 1), while the second simulation includes the added effect

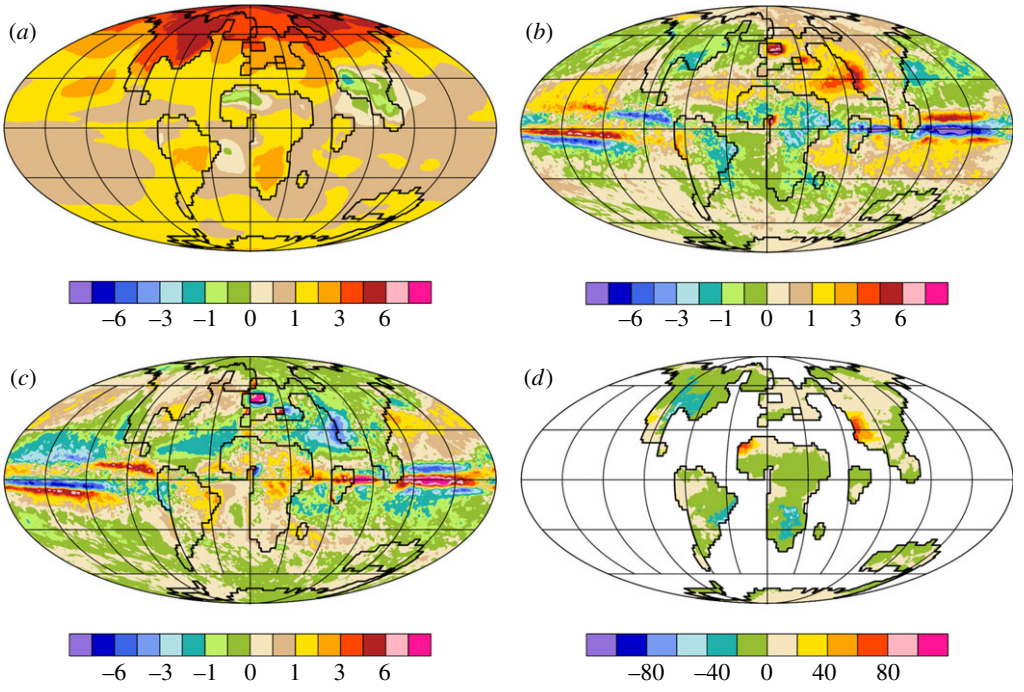

Figure 2. Change (ORBMAX-CONTROL) in annual mean (*a*) surface air temperature (°C), (*b*) precipitation (mm d^{-1}), (*c*) evaporation minus precipitation (mm d^{-1}) and (*d*) upper 1 m soil moisture (kg m^{-2}) due to orbital maximum insolation for the PETM versus control orbital insolation for the PETM.

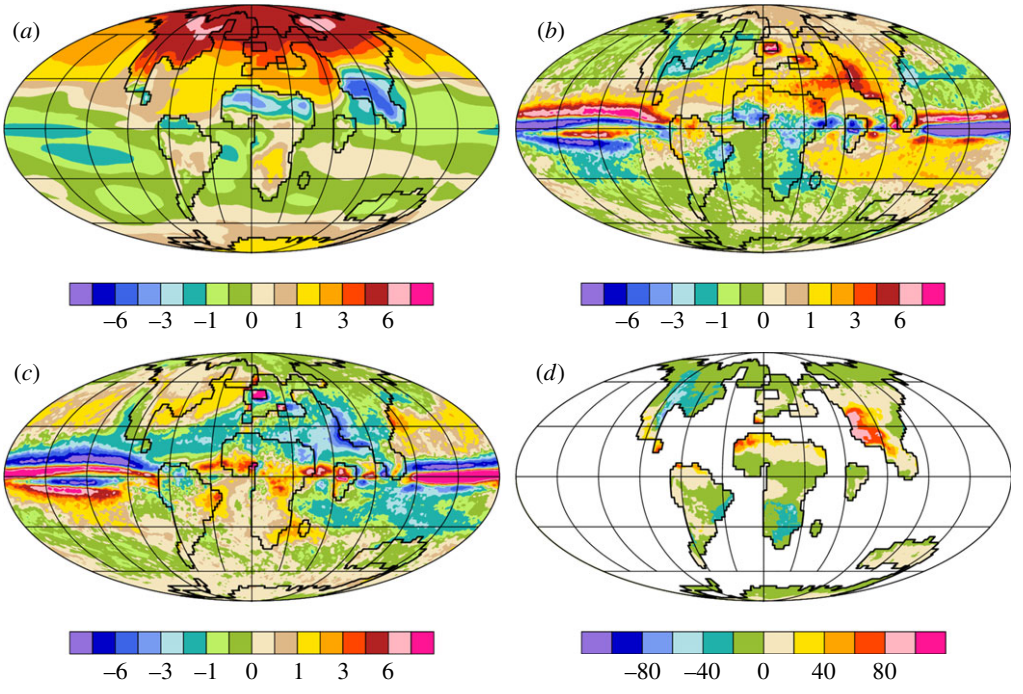

Figure 3. Change (ORBMAX-ORBMIN) in annual mean (*a*) surface air temperature (°C), (*b*) precipitation (mm d^{-1}), (*c*) evaporation minus precipitation (mm d^{-1}) and (*d*) upper 1 m soil moisture (kg m^{-2}) due to orbital maximum insolation for the PETM versus minimum orbital insolation for the PETM.

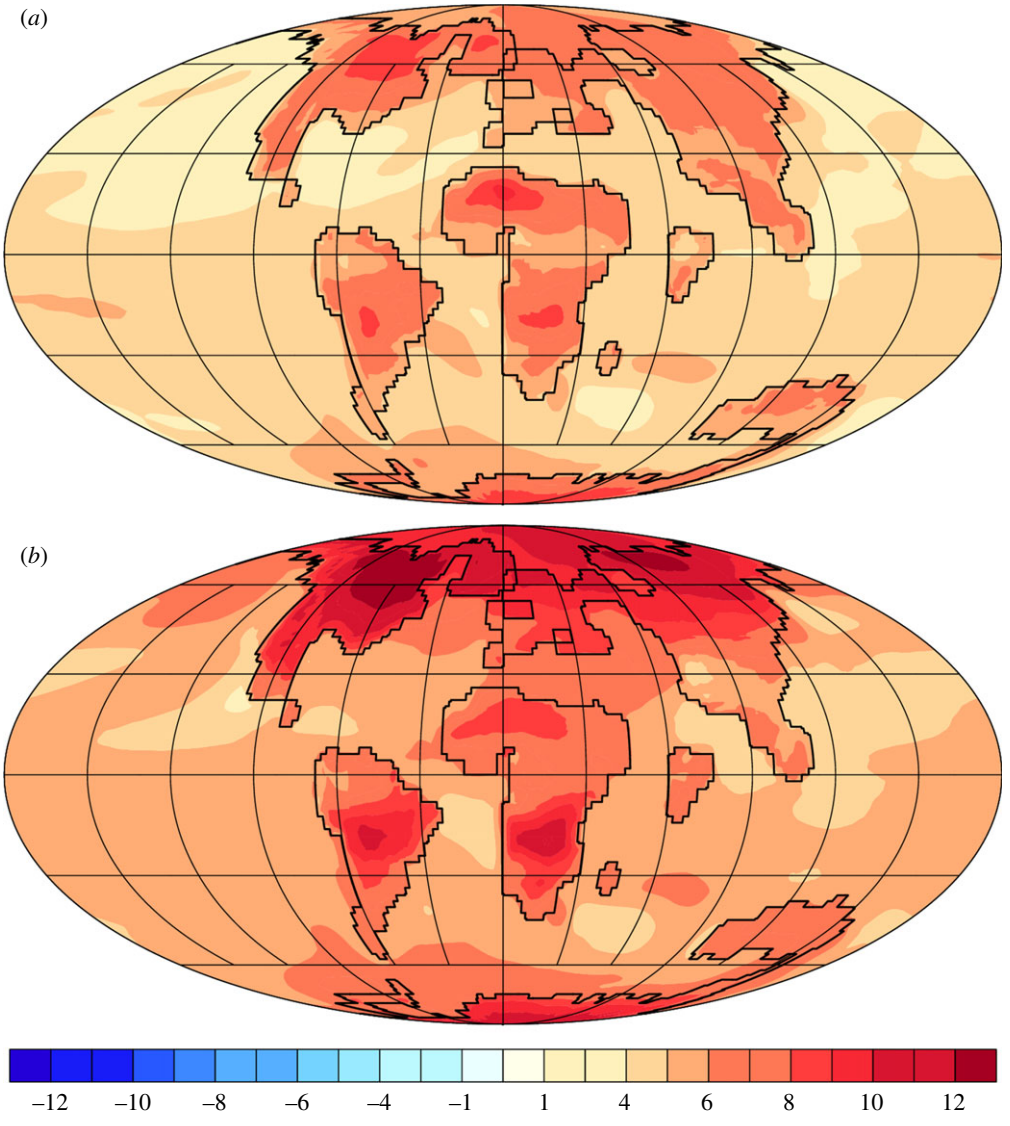

Figure 4. Change in annual mean surface air temperature (°C) for (*a*) greenhouse-forced PETM minus PRE-PETM and (*b*) greenhouse plus maximum orbital-forced PETM minus PRE-PETM.

of maximum solar orbital forcing (figure 1*a*). The changes in global surface air temperature for these two cases are shown in figure 4. Note that the two PETM cases are differenced off the same PRE-PETM simulation. Including maximum orbital forcing leads to enhanced surface warming, especially at high latitudes of both hemispheres. The additional warming is 4–5°C in magnitude. The change in precipitation due to adding orbital forcing is dramatic (figure 5). Over North America there is a shift from increased precipitation in the greenhouse-forced case to a large decrease in precipitation with the addition of maximum orbital forcing. The decrease in the North American precipitation is due to a weakening of moisture transport from the Pacific (due to a weaker latitudinal pressure gradient in the North Pacific) along with a decrease in local evaporation (approx. $10\,\mathrm{Wm}^{-2}$) and enhanced sensible heating from the surface (greater than $10\,\mathrm{Wm}^{-2}$). The increase in annual mean precipitation over eastern China is due mainly to an enhanced monsoonal circulation during summer months. Net availability of water at the surface is to a large extent determined by the difference between evaporation and precipitation

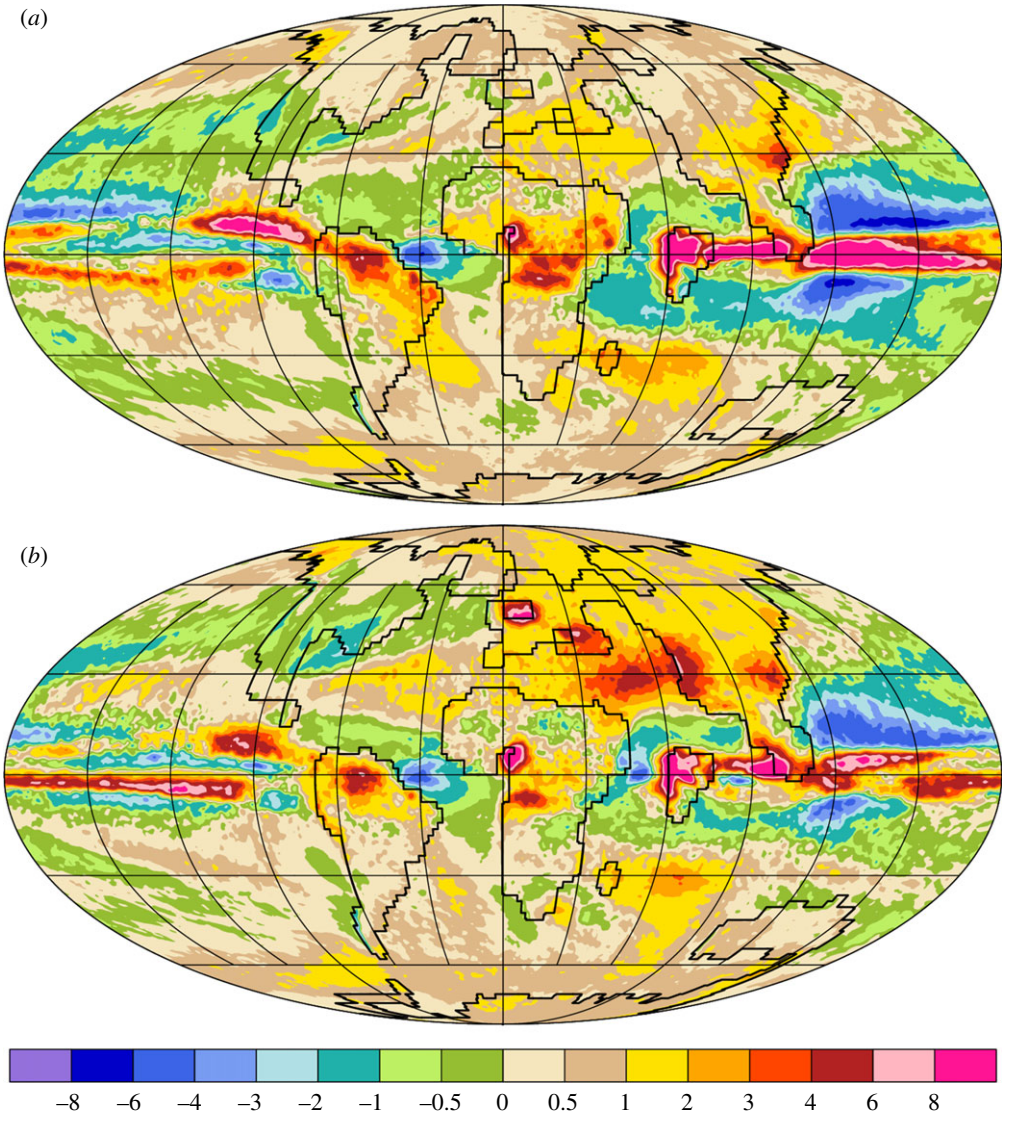

Figure 5. Change in annual mean precipitation (mm d^{-1}) for (*a*) greenhouse-forced PETM minus PRE-PETM and (*b*) greenhouse plus maximum orbital-forced PETM minus PRE-PETM.

(figure 6). The differences between the greenhouse-forced PETM and that including maximum orbital forcing reflects both local enhanced precipitation (P) and evaporative drying (E), where positive E-P denotes a drying of the surface, while negative E-P denotes moistening of the surface. Over oceans, subtropical evaporation exceeds precipitation, leading to higher salinity. Over land, these processes correlate with changes in the top 1 m level of soil moisture (figure 7). The change in soil moisture over mid- to upper latitude North America for maximum orbital forcing is negative compared with the case for greenhouse forcing, indicating enhanced evaporation due to additional surface warming.

(b) Regional seasonal response

As noted in the Introduction, palaeo-proxy data indicate enhanced seasonality at specific sites. Thus, it is important to not just consider annual or seasonal means, but also the seasonal cycle in climatic variables, e.g. [20]. The regional seasonal analysis is carried out for five regions where

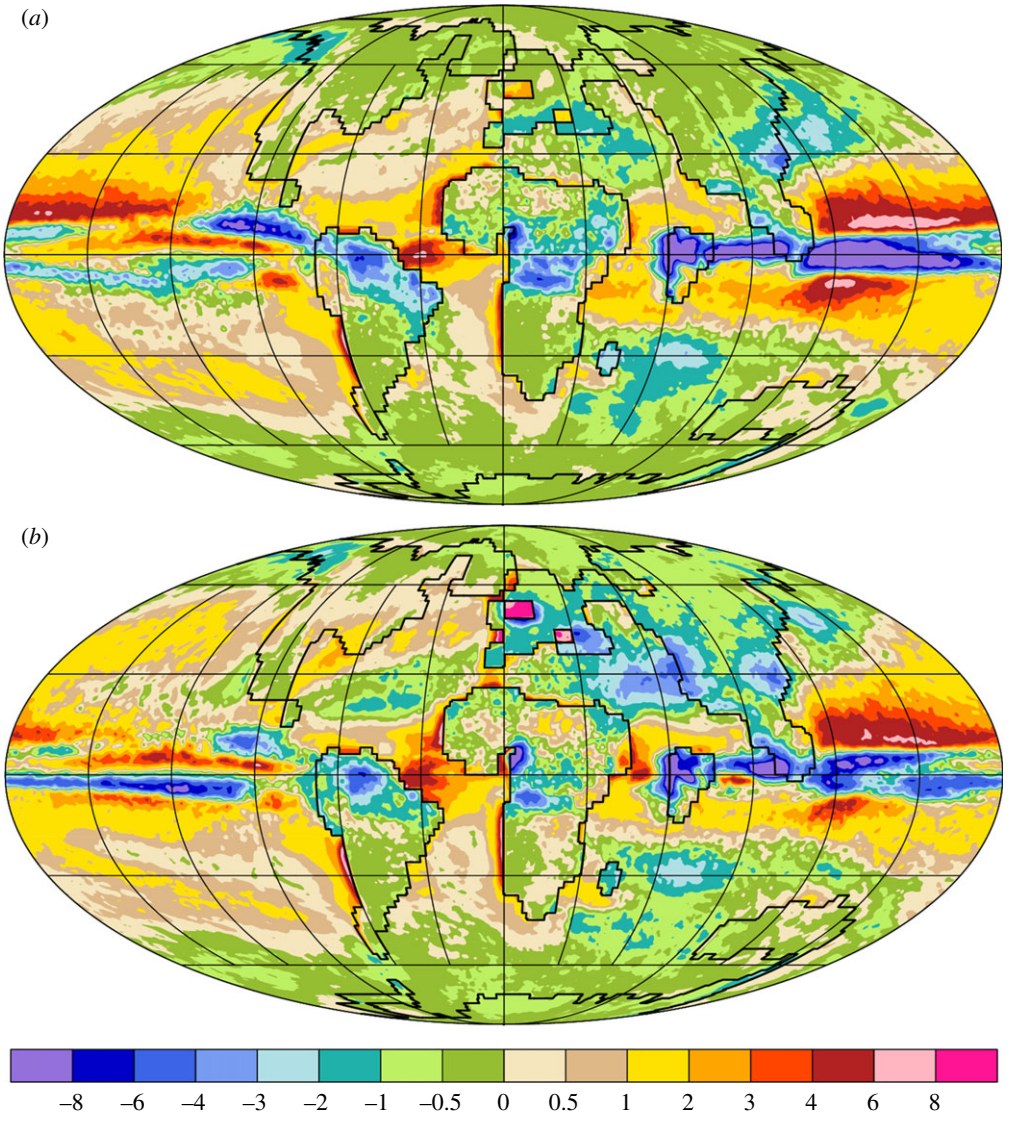

Figure 6. Change in annual mean evaporation minus precipitation (mm d^{-1}) for (*a*) greenhouse-forced PETM minus PRE-PETM and (*b*) greenhouse plus maximum orbital-forced PETM minus PRE-PETM.

palaeo-proxy data are available. The palaeo latitudes and longitudes for the five regions are summarized in table 2 and are denoted as: Bighorn Basin, New Jersey, Maryland, China and the Spanish Pyrenees in the following discussion.

Results are provided for four different scenarios from the half-degree CAM4 simulations: (i) PETM orbital maximum minus PETM orbital minimum forcing, (ii) PETM orbital maximum minus PETM, (iii) PETM orbital maximum minus PRE-PETM, and (iv) PETM minus PRE-PETM. Note that the PETM and PRE-PETM simulations both use modern orbital settings (table 1). The first case indicates the maximum Northern Hemisphere summer effect of orbital forcing for fixed greenhouse gas levels. The second case indicates the effects of maximum orbital forcing for the PETM climate. The third and fourth cases indicate climate change across the PETM boundary that include or exclude maximum orbital forcing, respectively. Changes in the seasonal cycle in mean surface air temperature, precipitation, evaporation minus precipitation and river run-off are presented for each region. For further clarification, we provide the seasonal cycle of absolute

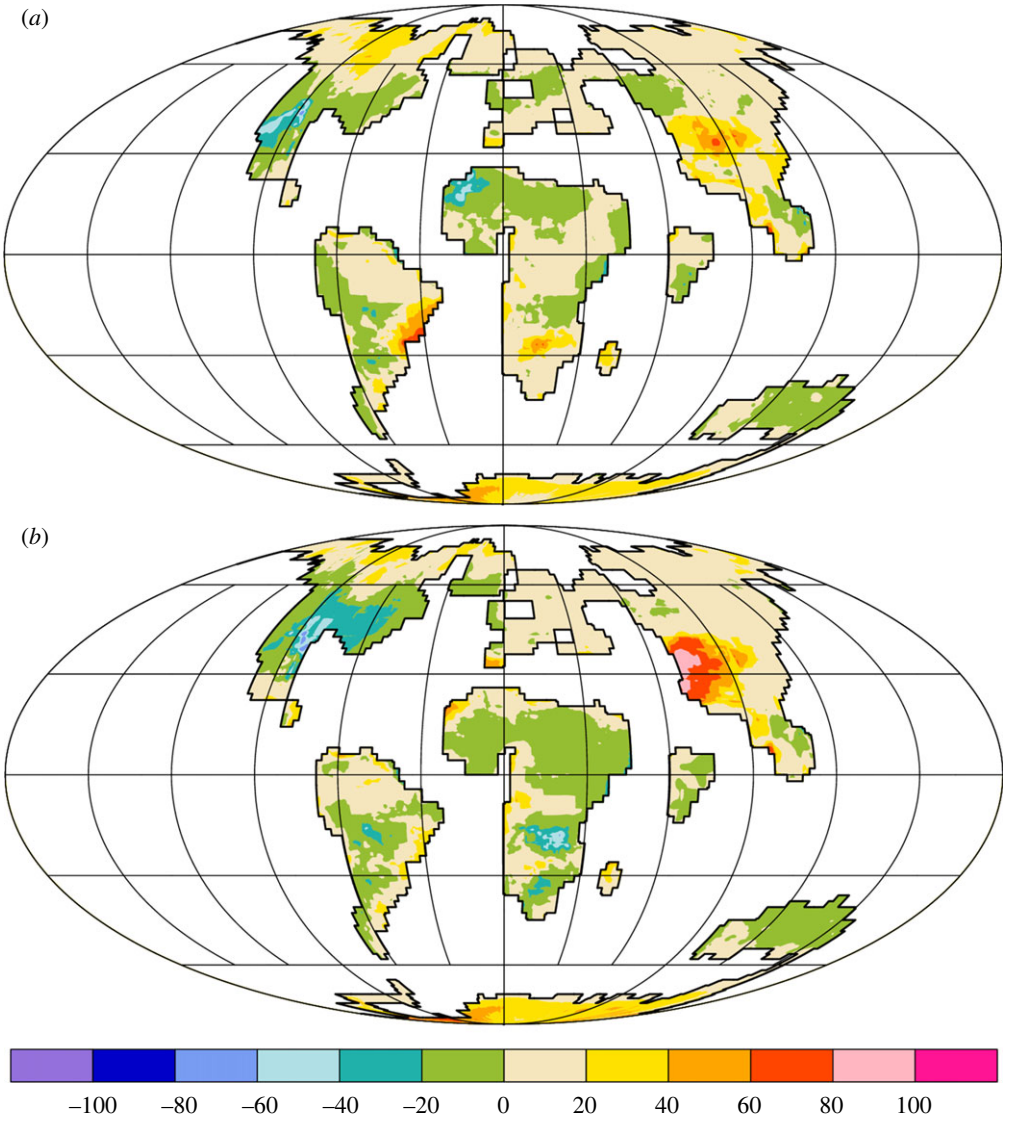

Figure 7. Change in annual mean upper 1 m soil moisture (kg m^{-2}) for (*a*) greenhouse-forced PETM minus PRE-PETM and (*b*) greenhouse plus maximum orbital-forced PETM minus PRE-PETM.

Table 2. Palaeo-coordinates for the five regions analysed in the present study.

region	latitude range (degrees)	longitude range (degrees)
Bighorn Basin	53–55 N	89–90 W
New Jersey	41–43 N	49–51 W
Maryland	40–42 N	52–54 W
China	30–32 N	110–112 E
Spanish Pyrenees	34.5–36.5 N	0–2 E

fields for each case and region in the electronic supplementary material. Following previous deep time orbital modelling studies [20–24], we do not adjust our model results for the calendar effect.

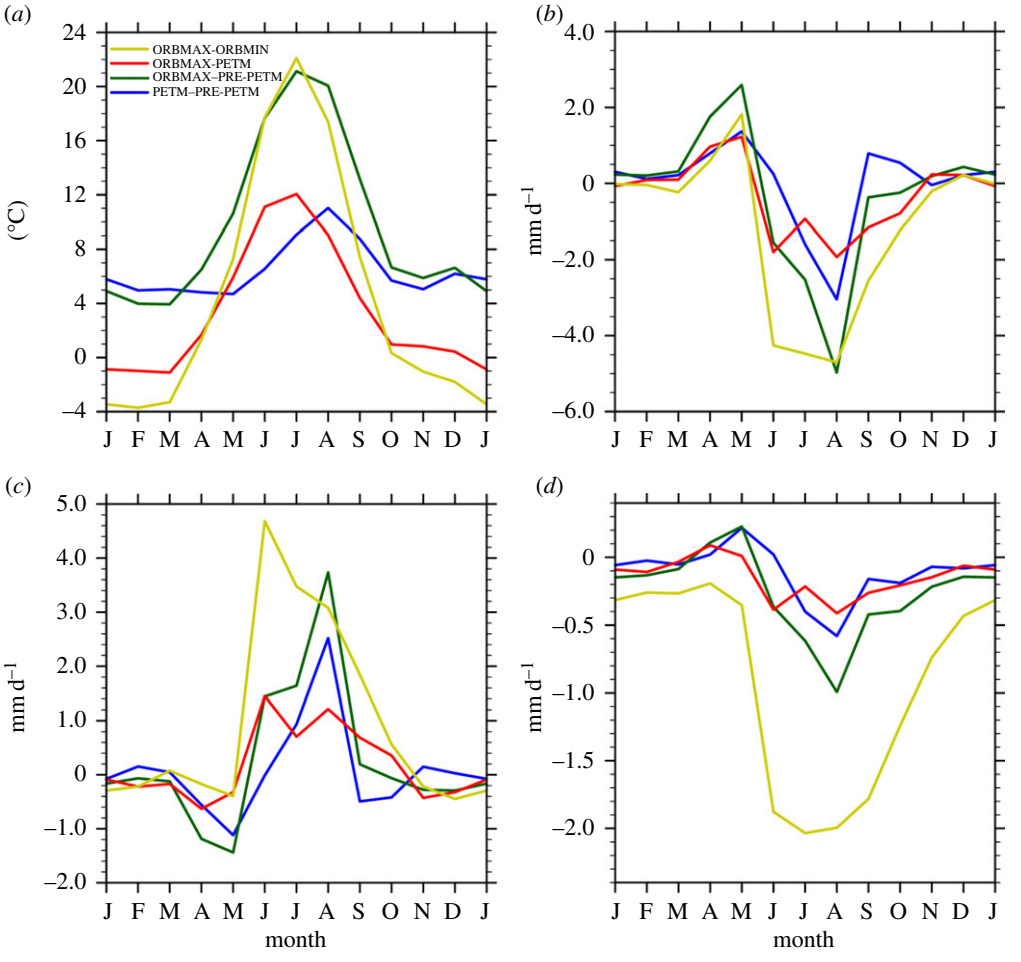

Figure 8. Bighorn Basin region. Annual cycle of (*a*) surface air temperature (°C), (*b*) precipitation (mm d^{-1}), (*c*) evaporation minus precipitation (mm d^{-1}), and (*d*) river run-off (mm d^{-1}) for PETM–PRE-PETM, maximum orbital forcing plus greenhouse forcing PETM–PRE-PETM, maximum orbital forcing plus greenhouse forcing PETM minus PETM, maximum–minimum orbital forcing for PETM.

(i) Bighorn Basin

The annual cycle of changes in surface air temperature for the Bighorn Basin (figure 8*a*) clearly show the importance of orbital forcing. For the case in which orbital forcing is fixed (blue), the change in surface temperature ranges from approximately 6°C from October to June to a maximum change of 11°C in August. When maximum orbital forcing is included, the maximum warming in July exceeds 20°C. Note that the change in temperature for the orbital maximum PETM minus PETM (red curve) is less than the PETM–PRE-PETM (blue curve) during the months of August to April, which is due to lower solar insolation at the latitude of the Bighorn Basin (figure 1*a*). The greatest range in seasonal temperatures occurs for the largest range in orbital forcing (yellow curve), i.e. maximum minus minimum orbital forcing. Changes in monthly mean precipitation for this region are similar for all four forcing cases with a decrease in precipitation for the months of May to October. This decrease is most probably due to a decrease in the local source of water and less transport of water vapour into the Bighorn Basin region. Model simulations of the mean annual precipitation for this region range from 700 to 1150 mm, which compare well with the observations presented in Kraus *et al.* [12] with a range of 1000–1400 mm. Wing *et al.*

Table 3. Bighorn Basin observed and modelled mean annual temperature, warm month mean, cold month mean and mean annual range in temperature. All values in °C. Observations are from Snell *et al.* [42].

	OBS PETM	PETM	Min PETM	Max PETM	OBS modern	CAM modern
MAT	20	20.8	19.4	24.4	7.8	4
WMM	34	40.9	31.8	53	22.4	22
CMM	5	5.9	8.5	5	−7.7	−11.5
MART	29	35	23.3	48	30.1	33.5

[11] report a value in mean annual precipitation of 800 mm for the drier PETM. With regard to the results in [20], Lawrence *et al.* simulate double maxima in the seasonal precipitation for this region. Our results (electronic supplementary material) also show this feature for our simulations. However, unlike [20], we simulate an increase in winter precipitation with warm orbital forcing, while the authors in [20] simulate a reduction. The changes in E-P (figure 8*c*) indicate significant late spring, early summer drying for the cases that include maximum orbital forcing compared with the case with greenhouse forcing by itself. Maximum drying for this region occurs for the greatest difference in orbital forcing (yellow curve). The change in simulated river run-off (figure 8*d*) for this region is strongly correlated with changes in local precipitation with significant reductions during late spring and summer. Again, the largest changes in run-off occur for the largest swing in orbital forcing (yellow curve). All cases exhibit strong seasonality in all four variables, which is symptomatic of interior continental regions. The model results also indicate that the phase of orbital forcing may have played a critical role in the Bighorn Basin hydrological cycle, a result supported by the observational findings of Abels *et al.* [40].

Palaeo-proxy data [12,41,42] indicate general drying in the Bighorn Basin at the onset of the PETM, followed by a gradual transition to wetter conditions, which is consistent with a shift in orbital forcing, i.e. cooler and wetter summers. All model simulations exhibit drying at the onset of the PETM (figure 8*c*), with the greatest drying occurring for the extremes in orbital forcing. We use the observations of Snell *et al.* [42] to evaluate the various model simulations of the PETM. The results are summarized in table 3.

The last two columns of table 3 compare the CAM-simulated modern-day metrics for temperature with observations. The model underestimates the modern mean annual temperature for this region, which is due mostly to simulating colder winter temperatures than observed. In terms of PETM simulations, the case that includes both maximum orbital and greenhouse forcing overestimates all temperature metrics except for the cold month mean temperature of 5°C. The cases that use either greenhouse forcing alone or greenhouse forcing and minimum orbital forcing are in closest agreement with observations.

(ii) North American eastern coast

North American east coast climatic shifts in seasonality are represented by the sites in New Jersey [7,43,44] and Maryland [45]. Both sites provide observational evidence for enhanced seasonality in the local hydrological cycle with enhanced river flow into the mid-latitude North Atlantic. Results for the New Jersey region are shown in figure 9. Again, we present changes in surface air temperature, precipitation, evaporation minus precipitation and river run-off. Most simulations show enhanced summer warming (figure 9*a*) with the orbital maximum minus minimum (yellow) exhibiting the greatest change in seasonality (approx. 12°C). The greenhouse only (blue) exhibits little seasonality in surface air temperature. In terms of the hydrological cycle the signals are highly variable for all cases; however, the maximum orbital plus greenhouse forcing versus the PRE-PETM (dark green) does show enhanced river run-off (figure 9*d*) from October to March (greater than 70%). Enhanced run-off also occurs for the greenhouse gas-forced case, but is smaller than the case that includes orbital forcing (approx. 50%). Note that the difference in

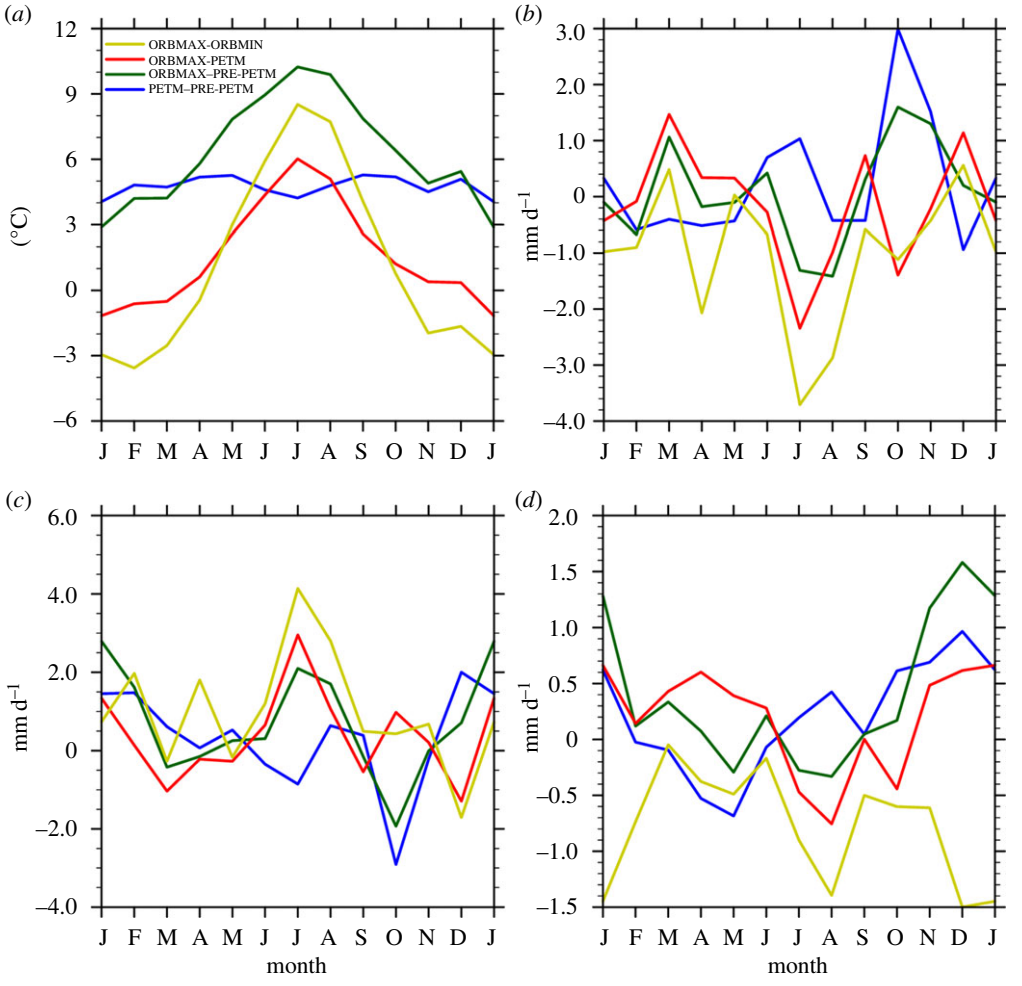

Figure 9. New Jersey region. Annual cycle of (*a*) surface air temperature (°C), (*b*) precipitation (mm d^{-1}), (*c*) evaporation minus precipitation (mm d^{-1}), and (*d*) river run-off (mm d^{-1}) for PETM–PRE-PETM, maximum orbital forcing plus greenhouse forcing PETM–PRE-PETM, maximum orbital forcing plus greenhouse forcing PETM minus PETM, maximum–minimum orbital forcing for PETM.

simulations that generates the greatest seasonality in surface temperature (maximum orbital forcing minus minimum forcing) (yellow) also simulates a significant decrease in river run-off. Similar conclusions apply to the Maryland site (figure 10). Seasonality in temperature change is enhanced with orbital forcing (figure 10*a*) and the largest enhancement in seasonal river run-off occurs for the case that includes both maximum orbital and greenhouse forcing (approx. 100%). The case with maximum orbital forcing for the PETM minus the PRE-PETM (figure 10*d*) shows a reduction in run-off of 20–50%.

(iii) Eastern Asia

Results from the eastern Asian region of modern-day China are shown in figure 11. Observations for this region by Chen *et al*. [46] indicate enhanced precipitation at the PETM boundary. Results from the simulation for the difference in precipitation for the PRE-PETM and PETM indicate enhanced precipitation (figure 11*b*) for the case of greenhouse forcing alone (blue) and those including maximum orbital forcing (dark green). Note that the seasonal peak in enhanced

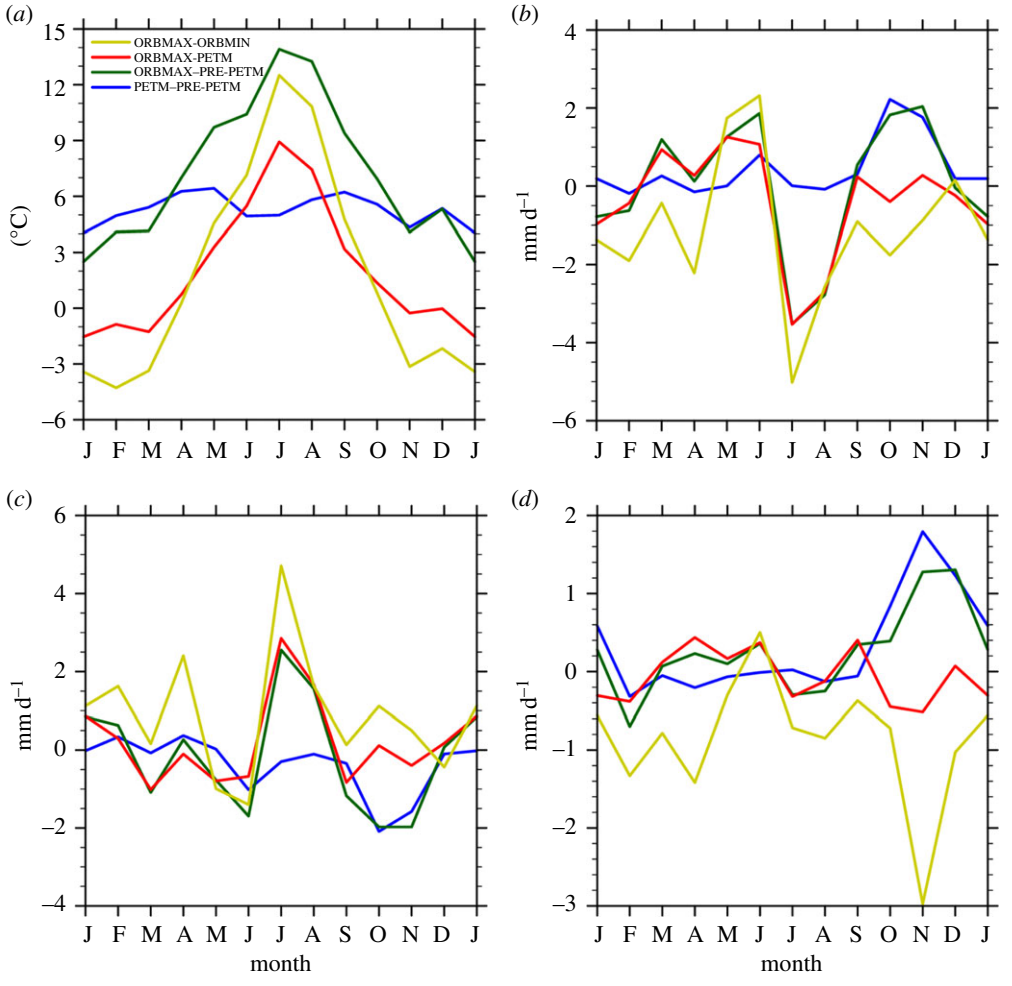

Figure 10. Maryland region. Annual cycle of (*a*) surface air temperature (°C), (*b*) precipitation (mm d^{-1}), (*c*) evaporation minus precipitation (mm d^{-1}), and (*d*) river run-off (mm d^{-1}) for PETM–PRE-PETM, maximum orbital forcing plus greenhouse forcing PETM–PRE-PETM, maximum orbital forcing plus greenhouse forcing PETM minus PETM, maximum–minimum orbital forcing for PETM.

precipitation occurs in September for greenhouse gas forcing, while it takes place in May and June for the case that includes orbital forcing. The enhancement in precipitation is greater than that due to evaporation (figure 11*c*), leading to a net enhanced run-off for these two cases (figure 11*d*). The cases with the same fixed levels of PETM greenhouse forcing (yellow and red curves) indicate that orbital forcing increases the seasonal amplitude of surface temperature, precipitation and run-off (figure 11*a*,*b*,*d*). As noted, these results are consistent with the proxy data that indicate enhanced precipitation in this region at the PETM.

What causes this increase in precipitation for the east China region? Analysis of the water cycle indicates that an active atmospheric river extending from the tropical proto-Indian Ocean supplies much of the moisture for this enhancement. Analysis of the climatology of water vapour transport into eastern China identifies three main atmospheric rivers (figure 12). One river has landfall centred at 35° N (figure 12*a*), another river has landfall centred at 45° N (figure 12*b*) and a third river has landfall centred at 50° N (figure 12*c*). A statistical analysis of the seasonality of the atmospheric rivers for this region (figure 13) indicates peak moisture transport from November to April. The analysis also indicates that the inclusion of maximum orbital forcing in addition to greenhouse forcing leads to increased moisture transport in local summer.

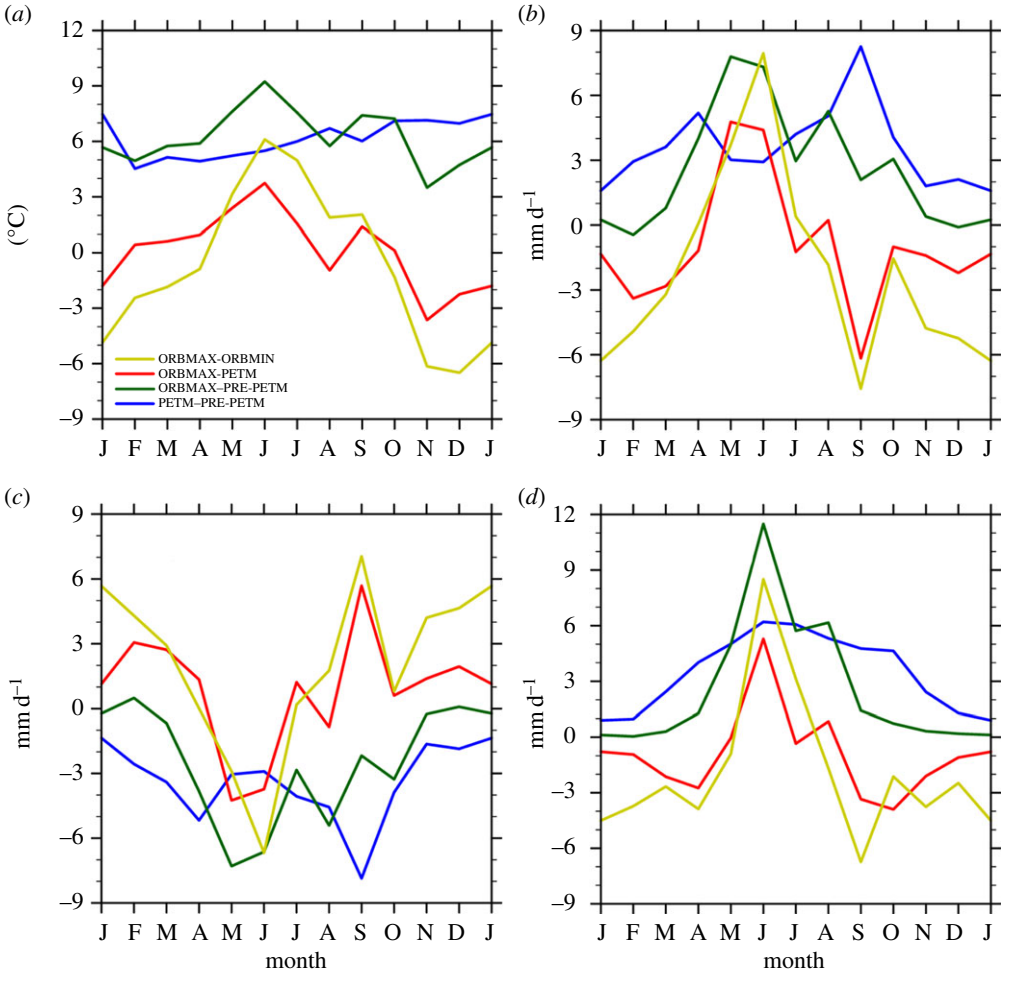

Figure 11. China region. Annual cycle of (*a*) surface air temperature (°C), (*b*) precipitation (mm d^{-1}), (*c*) evaporation minus precipitation (mm d^{-1}), and (*d*) river run-off (mm d^{-1}) for PETM–PRE-PETM, maximum orbital forcing plus greenhouse forcing PETM–PRE-PETM, maximum orbital forcing plus greenhouse forcing PETM minus PETM, maximum–minimum orbital forcing for PETM.

(iv) Spanish Pyrenees

The seasonal analysis for the Spanish Pyrenees region (table 2) is shown in figure 14. Proxy data for this region [10,47] provide evidence for increased precipitation and fluvial flow at the onset of the PETM. Similar to the other regions, the Pyrenees experienced enhanced seasonal amplitude in surface air temperature across the PETM boundary (figure 14*a*, blue and dark green curves), in which the inclusion of maximum orbital forcing increases summer warming by 8°C above that due to greenhouse forcing. Seasonal precipitation also increases for these two cases (figure 14*b*) with maximum increase in rainfall occurring from October to January with increases for PETM–PRE-PETM differences of 50–200%, and for the ORBMAX-ORBMIN differences of 100–150%. Amplified seasonal surface temperature increases summer evaporation leading to excessive drying for June, July and August (figure 14*c*). The case with combined greenhouse and maximum orbital forcing predicts the largest increase in river run-off in August, September and October (figure 14*d*, dark green curve) compared with the greenhouse-forced case (figure 14*d*, blue curve). Overall, both cases predict increased river run-off during the onset of the PETM in concert

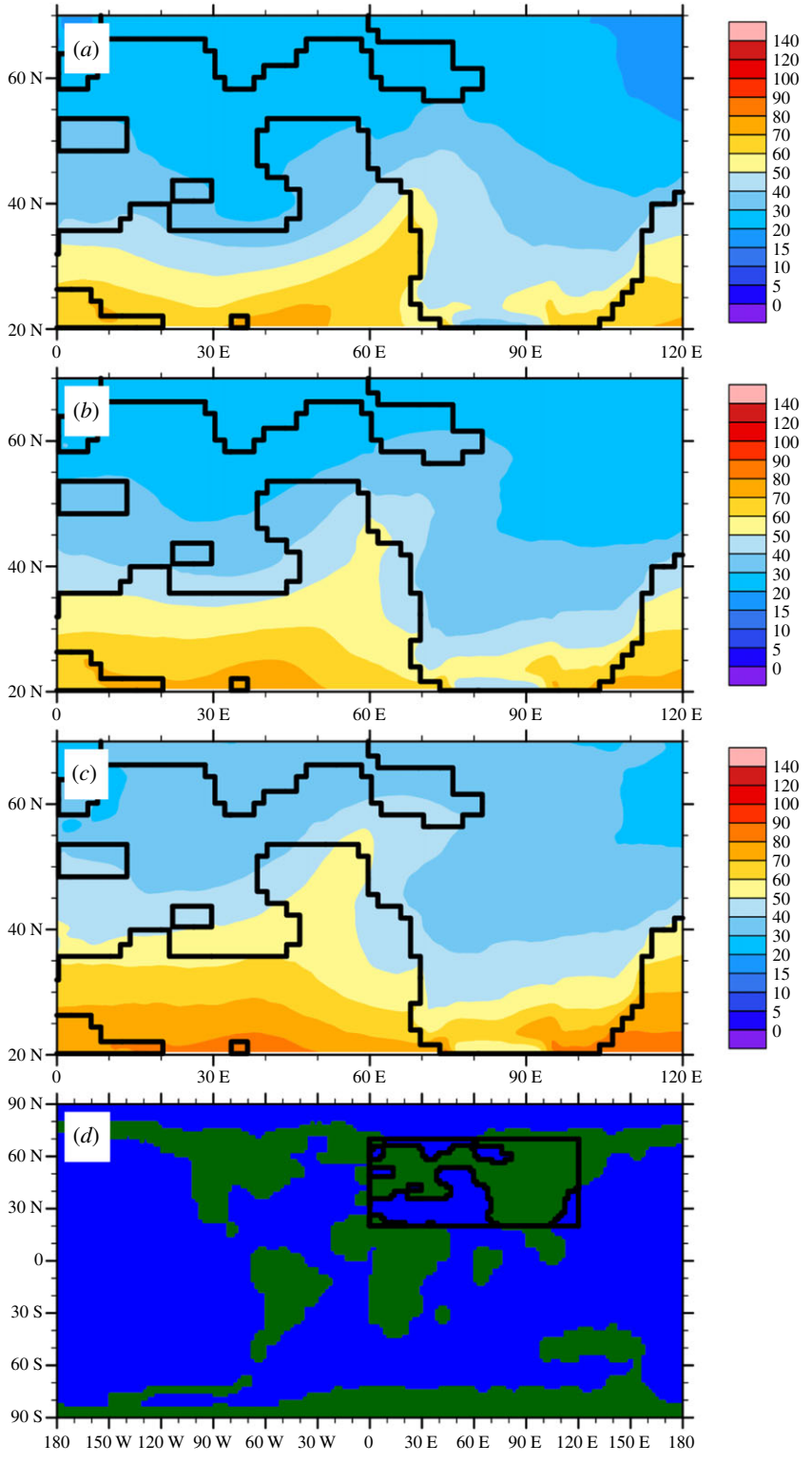

Figure 12. Atmospheric river (AR) composite for east Asia for three landfalling regions (*a–c*) of landfall. Total column integrated water vapour is plotted (kg m^{-2}). Composites are calculated by averaging all AR events for the given latitude range of 32–40° N (*a*), 40–50° N (*b*), 50–60° N (*c*). A global view is shown (*d*) for the palaeogeographic context highlighting the Asian AR region with a black box and thickened continental outlines.

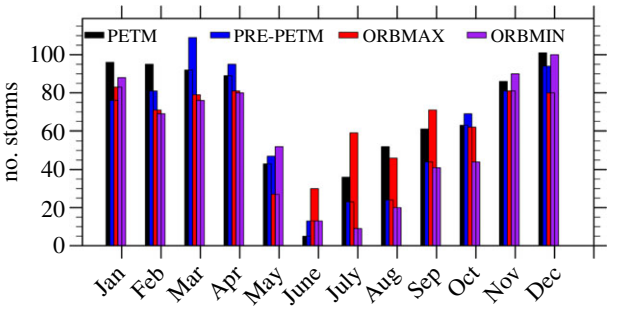

Figure 13. Annual cycle in the number of storms over a 20-year period related to Asian atmospheric rivers for four cases: PETM (black), maximum orbital PETM (red), PRE-PETM (blue) and minimum orbital PETM (purple). Individual storms were determined by aggregating consecutive 6 h periods. The AR detection algorithm used for this study applies a series of geographical and geometric characteristics, as well as low-level wind and moisture data, to detect landfalling AR events every 6 h. Full details can be found in Shields & Kiehl [37,38].

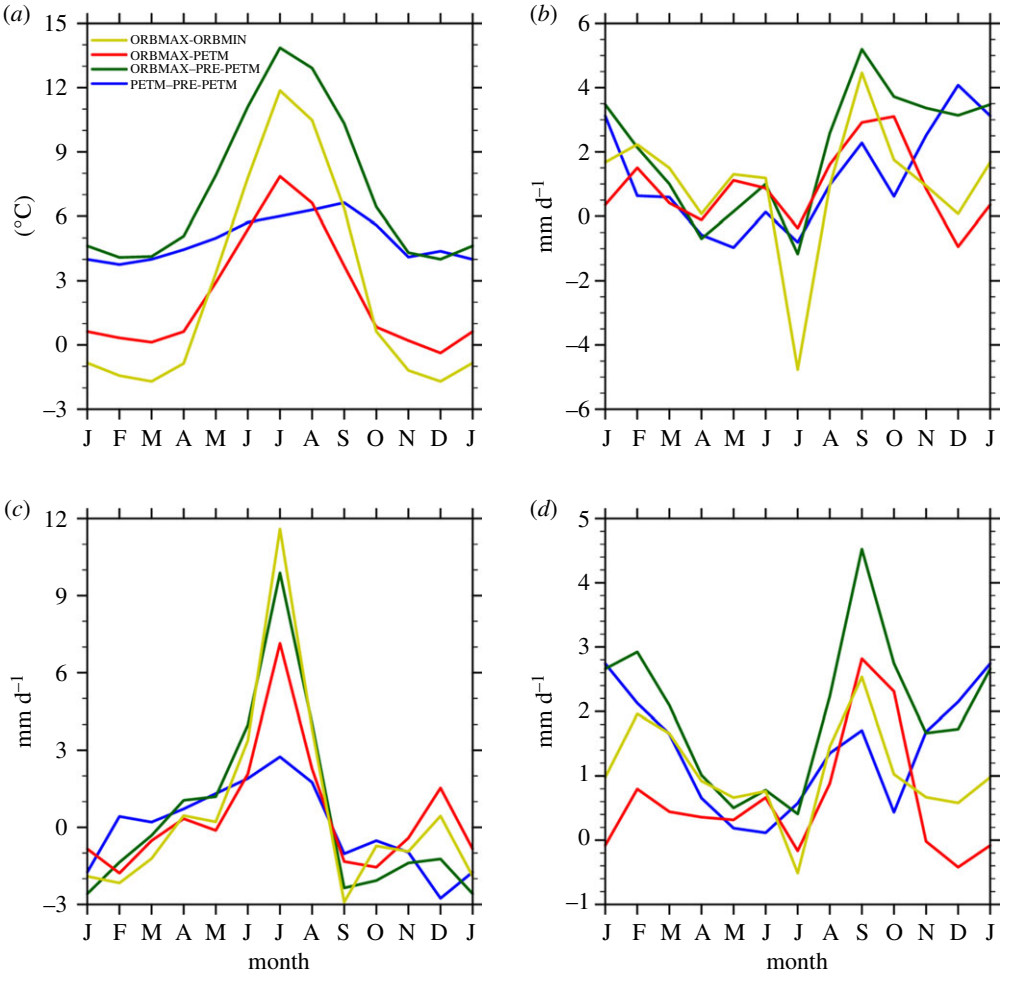

Figure 14. Spanish Pyrenees. Annual cycle of (*a*) surface air temperature (°C), (*b*) precipitation (mm d^{-1}), (*c*) evaporation minus precipitation (mm d^{-1}) and (*d*) river run-off (mm d^{-1}) for PETM–PRE-PETM, maximum orbital forcing plus greenhouse forcing PETM–PRE-PETM, maximum orbital forcing plus greenhouse forcing PETM minus PETM, maximum–minimum orbital forcing for PETM.

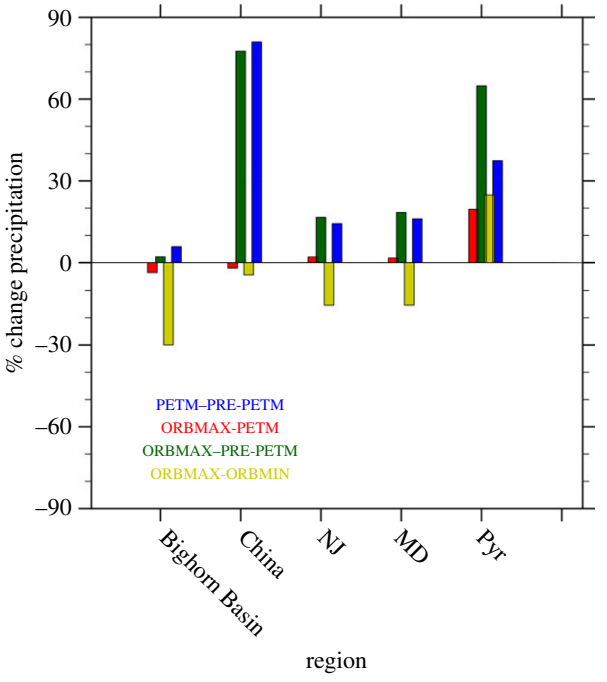

Figure 15. Normalized per cent change in the 95th percentile in precipitation for regions listed for PETM– PRE-PETM, maximum orbital forcing plus greenhouse forcing PETM – PRE-PETM, maximum orbital forcing plus greenhouse forcing PETM minus PETM, maximum–minimum orbital forcing for PETM.

with the proxy data. The remaining two cases considering the role of orbital forcing during the PETM present similar results to those across the PETM boundary.

(c) Extreme events

The general conclusion from the regional analysis is that seasonality in temperature and the hydrological cycle increased across the PETM boundary. Simulations that include orbital forcing enhance this signal over that of a purely greenhouse-forced event. It is important to recognize that the increase in seasonality does not occur uniformly, but is accompanied by a significant increase in extreme events. Essentially, as the mean of temperature and hydrological variables increases, the tails of the distribution of these variables also shift to higher values, which implies more frequent extremes. To quantitatively assess this phenomenon, the relative shift in the 95th percentile of daily precipitation was calculated for each of the five regions (figure 15). For the cases that consider changes in variables across the PETM boundary (blue, dark green bars) a significant increase in extreme precipitation is predicted for China (approx. 80%) and the Spanish Pyrenees (30% and 60%), while the remaining regions show more modest increases in extreme daily precipitation (10−20%) across the PETM boundary. The case with maximum minus minimum orbital forcing for the PETM (figure 15, yellow bar) indicates a decrease in extreme precipitation for all regions except for the Spanish Pyrenees. This difference in response to changes in orbital forcing is due to the seasonal peak in precipitation in the Spanish Pyrenees region compared with the other regions. The peak in precipitation for the Pyrenees occurs in August–September, while for the other regions it is in the winter time. Figure 1*b* indicates that the reduction in solar insolation is greatest in the winter months at mid-latitudes, while for August–September there is enhanced solar forcing at mid-latitudes. Thus, the changes shown in figure 15 result from the negative solar forcing that occurs during peak seasonal precipitation for the Bighorn Basin, NJ, MD and China, but not for the Spanish Pyrenees. Extremes in run-off are in general agreement

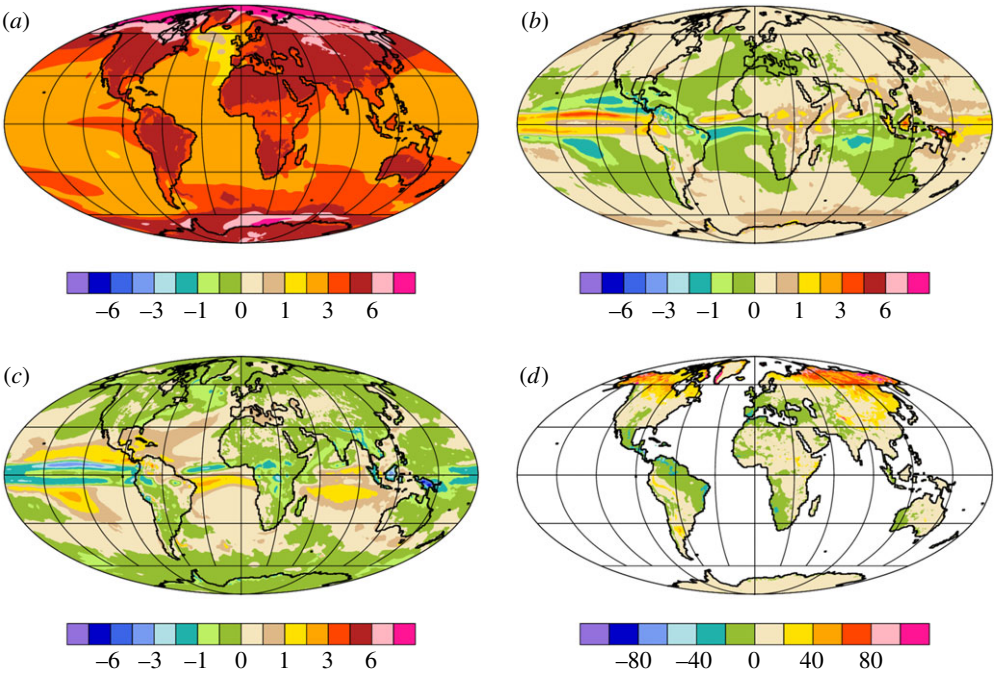

Figure 16. Change in (*a*) surface air temperature (°C), (*b*) precipitation (mm d^{-1}), (*c*) evaporation minus precipitation (mm d^{-1}), and (*d*) upper 1 m soil moisture (kg m^{-2}) from the end of the RCP8.5 twenty-first century versus end of the twentieth century.

with the local extremes in daily precipitation. Thus, the model results support the observational data indicating that excessive fluvial transport took place in these regions at the onset of the PETM.

(d) Relation to future climate response

Given that the PETM was a climate transition forced mainly by changes in greenhouse gases, it is of interest to consider how the changes simulated for PETM compare with projected future climate change due to increased greenhouse forcing. To carry out this comparison, we employ coupled model CCSM (v. 4) simulations for the twenty-first century that employ a 0.5° atmosphere/land resolution and 1° ocean/sea-ice resolution [21]. The twenty-first century simulation is a continuation of a transient CCSM simulation for the twentieth century. The model simulation employs the IPCC RCP8.5 forcing scenario [48]. The geographical distributions of annual mean change in surface air temperature, precipitation, evaporation minus precipitation and soil moisture are shown in figure 16. Note these results are from a transient climate simulation and do not reflect equilibrium changes in these climate variables. All previously discussed simulations in this study for the PETM use conditions close to climatic equilibrium. Thus, the transient twenty-first century climate response is less than that expected for a case in which greenhouse and aerosol forcings are held fixed at 2100 levels and the model is run to a near-equilibrium state. The differences shown in figure 16 are calculated by comparing the average of the last 20 years of the twenty-first century with the average results from the end of the twentieth century.

Changes in annual surface air temperature over continental regions range from 4°C to 6°C, while changes over ocean regions are for the most part 3–5°C, again indicative of the transient lag in ocean warming compared with land warming. These changes are similar in magnitude, but less than for the PETM minus PRE-PETM simulation (figure 4*a*). Changes in precipitation (figure 16*b*)

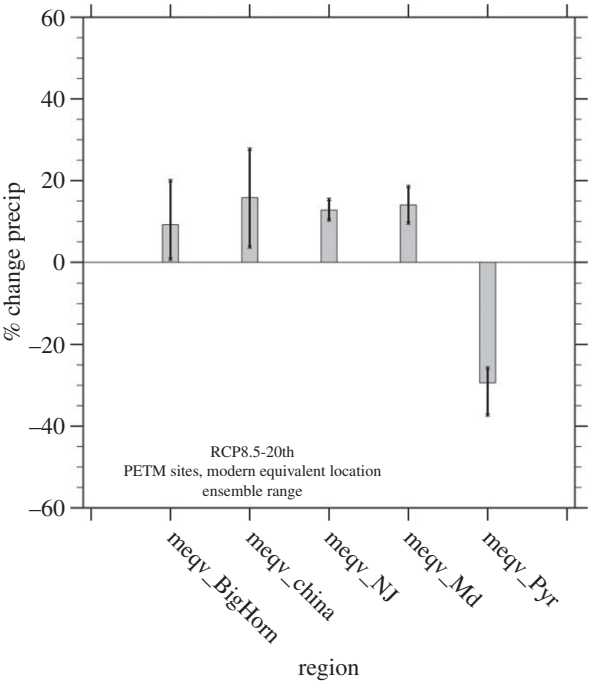

Figure 17. Normalized percent change in the 95th percentile in precipitation for regions listed for the end of the RCP8.5 twenty-first century versus end of the twentieth century.

over North America indicate a projected increase of approximately 0.5 mm d^{-1}, except for the extreme south-central west portion of North America, which projects a decrease in precipitation of similar magnitude. The PETM boundary change in precipitation (figure 5*a*) shows a similar signal. As noted, if maximum orbital forcing is included (figure 5*b*), then precipitation decreases over much of North America. Changes in continental evaporation minus precipitation (figure 16*c*) for the end of the twenty-first century are very similar in geographical distribution and magnitude when compared with the change for the PETM (figure 6*a*). Changes over ocean regions are dissimilar mainly due to the differences in SSTs related to the fact that the twenty-first century SSTs are not in an equilibrium state. Differences over ocean regions are also due to the fact that the PETM CAM simulations employ fixed SSTs, which implies more cooling due to an unlimited supply of water to evaporate. Finally, changes in simulated upper level soil moisture content at the end of the twenty-first century (figure 16*d*) differ over North America compared with the PETM (figure 7*a*), while they are similar in Asia with a large-scale increase of soil moisture over Asia.

Changes in extreme daily precipitation for the equivalent regions used in the above palaeo-analysis (figure 17) indicate increases of 10–20% for all regions except the Spanish Pyrenees, which experiences a 30% decrease in 95th percentile daily precipitation by 2100. The changes for the PETM–PRE-PETM case indicate similar increases in the Bighorn Basin, New Jersey and Maryland, but not for China or the Spanish Pyrenees. In China, the increase in extreme precipitation is 80%, compared with the future change of 20%, while the change in the Pyrenees for the PETM is an increase of 40%. The difference for the eastern China region is mainly due to differences in geography, in which for the early Eocene there was a direct atmospheric river connection to this region from the proto-Indian Ocean—a situation that clearly does not exist with present-day continental geography. The difference for the Spanish Pyrenees is related, again, to atmospheric rivers for, when considering the composites of ARs, there is significantly more moisture transport and variability during modern summer time.

5. Conclusion

We have used the high-resolution (50 km) CAM4 along with SSTs from fully coupled simulations to study changes in seasonal and extreme events associated with the onset of the PETM. We have also compared and contrasted the effects of including orbital forcing along with greenhouse forcing across the PETM. The basic conclusions are that for most regions (Bighorn Basin, China and the Spanish Pyrenees, in particular) increased greenhouse forcing enhances both the seasonality of temperature and the regional water cycle and that these changes are further enhanced by including maximum insolation in Northern Hemisphere summer. Five regions were studied and compared with palaeo-proxy studies to show that the model in general captures the observed shifts in temperature and enhanced water cycle at the PETM boundary. For example, the interior North American site at Bighorn Basin dries out at the onset of the PETM, and this drying is enhanced due to locally enhanced forcing from orbital effects. The region in China experiences a dramatic enhancement in precipitation and run-off at the PETM with enhancement through the inclusion of maximum insolation in Northern Hemisphere summer along with greenhouse forcing. These results are supported by the proxy data that indicate enhanced river transport at the PETM.

Comparison of the PETM simulations with future changes in Earth's climate system due to increased anthropogenic greenhouse forcing indicates similarities in continental warming. The future simulations also predict enhanced extremes in precipitation for all of the regions excluding the Spanish Pyrenees, where changes in moisture transport are different from the PETM simulations. The magnitude of increased extreme precipitation is considerably larger for the PETM simulations (as large as 70%) than for the future (as large as 20%).

These results indicate the usefulness of high-spatial resolution in studying Earth's water cycle. Future simulations are underway for global 25 km horizontal resolution simulations of the Earth's deep past climates. It is hoped that other modelling groups will carry out these types of simulations so that model ensemble results can be created for Earth's past climate states.

Data accessibility. Model output can be obtained upon request. Please contact J.T.K.

Authors' contributions. J.T.K., C.A.S., J.C.Z. and M.A.S. made substantial contributions to the conception and design of the study, and analysis and interpretation of data. M.R. made substantial contributions to the model configuration, and implementation and completion of model simulations. J.T.K., C.A.S. and J.C.Z. drafted the article for important intellectual content; and J.T.K. made the final approval of the version to be published.

Competing interests. We have no competing interests.

Funding. This work was supported by a grant from the Heising-Simons Foundation. The National Center for Atmospheric Research is sponsored by the National Science Foundation.

Acknowledgements. The authors thank anonymous reviewers for their constructive comments, which led to a number of improvements in the manuscript.

References

1. Kennett JP, Stott LD. 1991 Abrupt deep-sea warming, palaeoceanographic changes and benthic extinctions at the end of the Palaeocene. *Nature* **353**, 225–229. (doi:10.1038/353225a0)
2. Sluijs A *et al.* 2006 Subtropical Arctic ocean temperatures during the Palaeocene/Eocene Thermal Maximum. *Nature* **441**, 610–613. (doi:10.1038/nature04668)
3. Tripati A, Elderfield H. 2005 Deep-sea temperature and circulation changes at the Paleocene-Eocene Thermal Maximum. *Science* **308**, 1894–1898. (doi:10.1126/science.1109202)
4. Zachos JC, Schouten S, Bohaty S, Quattlebaum T, Sluijs A, Brinkhuis H, Gibbs SJ, Bralower TJ. 2006 Extreme warming of mid-latitude coastal ocean during the Paleocene-Eocene Thermal Maximum: inferences from TEX86 and isotope data. *Geology* **34**, 737–740. (doi:10.1130/G22522.1)
5. Zachos JC, Wara MW, Bohaty S, Delaney ML, Petrizzo MR, Brill A, Bralower TJ, Premoli-Silva I. 2003 A transient rise in tropical sea surface temperature during the Paleocene-Eocene Thermal Maximum. *Science* **302**, 1551–1554. (doi:10.1126/science.1090110)

6. Foreman BZ, Heller PL, Clementz MT. 2012 Fluvial response to abrupt global warming at the Palaeocene/Eocene boundary. *Nature* **491**, 92–95. (doi:10.1038/nature11513)
7. John CM, Bohaty SM, Zachos JC, Sluijs A, Gibbs S, Brinkhuis H, Bralower TJ. 2008 North American continental margin records of the Paleocene-Eocene Thermal Maximum: implications for global carbon and hydrological cycling. *Paleoceanography* **23**, PA2217. (doi:10.1029/2007PA001465)
8. Pagani M *et al.* 2006 Arctic hydrology during global warming at the Palaeocene/Eocene Thermal Maximum. *Nature* **443**, 598. (doi:10.1038/nature05211)
9. Robert C, Kennett JP. 1994 Antarctic subtropical humid episode at the Paleocene-Eocene boundary—clay-mineral evidence. *Geology* **22**, 211–214. (doi:10.1130/0091-7613(1994)022<0211:ASHEAT>2.3.CO;2)
10. Schmitz B, Pujalte V. 2007 Abrupt increase in seasonal extreme precipitation at the Paleocene-Eocene boundary. *Geology* **35**, 215–218. (doi:10.1130/G23261A.1)
11. Wing SL, Harrington GJ, Smith FA, Bloch JI, Boyer DM, Freeman KH. 2005 Transient floral change and rapid global warming at the Paleocene-Eocene boundary. *Science* **310**, 993–996. (doi:10.1126/science.1116913)
12. Kraus MJ, McInerney FA, Wing SL, Secord R, Baczynski AA, Bloch JI. 2013 Paleohydrologic response to continental warming during the Paleocene-Eocene thermal maximum, Bighorn Basin, Wyoming. *Palaeogeogr. Palaeoclimatol. Palaeoecol.* **370**, 196–208. (doi:10.1016/j.palaeo.2012.12.008)
13. Carmichael MJ *et al.* 2017 Hydrological and associated biogeochemical consequences of rapid global warming during the Paleocene-Eocene Thermal Maximum. *Global Planet. Change* **157**, 114–138. (doi:10.1016/j.gloplacha.2017.07.0144)
14. Lourens LJ, Sluijs A, Kroon D, Zachos JC, Thomas E, Rohl U, Bowles J, Raffi I. 2005 Astronomical pacing of late Palaeocene to early Eocene global warming events. *Nature* **435**, 1083–1087. (doi:10.1038/nature03814)
15. Westerhold T, Rohl U, Laskar J. 2012 Time scale controversy: accurate orbital calibration of the early Paleogene. *Geochem. Geophys. Geosyst.* **13**. (doi:10.1029/2012GC004096)
16. Westerhold T, Rohl U, McCarren HK, Zachos JC. 2009 Latest on the absolute age of the Paleocene-Eocene Thermal Maximum (PETM): new insights from exact stratigraphic position of key ash layers + 19 and-17. *Earth Planet. Sci. Lett.* **287**, 412–419. (doi:10.1016/j.epsl.2009.08.027)
17. Zachos JC, McCarren H, Murphy B, Röhl U, Westerhold T. 2010 Tempo and scale of late Paleocene and early Eocene carbon isotope cycles: implications for the origin of hyperthermals. *Earth Planet. Sci. Lett.* **299**, 242–249. (doi:10.1016/j.epsi.2010.09.004)
18. Galeotti S *et al.* 2010 Orbital chronology of early Eocene hyperthermals from the Contessa Road section, central Italy. *Earth Planet. Sci. Lett.* **290**, 192–200. (doi:10.1016/j.epsl.2009.12.021)
19. Zeebe RE, Westerhold T, Littler K, Zachos JC. 2017 Orbital forcing of the Paleocene and Eocene carbon cycle. *Paleoceanography* **32**, 440–465. (doi:10.1002/2016PA003054)
20. Lawrence KT, Sloan LC, Sewall JO. 2003 Terrestrial climatic response to precessional orbital forcing in the Eocene. In *Causes and consequences of globally warm climates in the early paleogene* (eds SL Wing, PD Gingrich, B Schmitz, E Thomas), pp. 65–77. Boulder, CO: Geo. Soc. Amer. Special Paper 369.
21. Sloan LC, Huber M. 2001 Eocene oceanic responses to orbital forcing on precessional time scales. *Paleoceanography* **16**, 101–111. (doi:10.1029/1999PA000491)
22. Keery JS, Holden PB, Edwards NR. 2018 Sensitivity of the Eocene climate to CO_2 and orbital variability. *Clim. Past. Discuss.* **14**, 215–238. (doi.10.5194/cp-2017-60)
23. DeConto RM, Galeotti S, Pagani M, Tracy D, Schaefer K, Zhang T, Pollard D, Beerling DJ. 2012 Past extreme warming events linked to massive carbon release from thawing permafrost. *Nature* **484**, 87–91. (doi:10.1038/nature10929)
24. Lunt DJ, Ridgwell A, Sluijs A, Zachos J, Hunter S, Haywood A. 2011 A model for orbital pacing of methane hydrate destabilization during the Palaeogene. *Nat. Geosci.* **4**, 775–778. (doi:10.1038/NGEO1266)
25. Meehl G, Tebaldi C. 2004 More intense, more frequent, longer lasting heat waves in the 21st century. *Science* **305**, 994–997. (doi:10.1126/science.1098704)
26. Stott P. 2016 How climate change affects extreme weather events. *Science* **352**, 1517–1518. (doi:10.1126/science.aaf7271)

27. Shields CA, Kiehl JT, Meehl GA. 2016 Future changes in regional precipitation simulated by a half-degree coupled climate model: sensitivity to horizontal resolution. *J. Adv. Model. Earth Syst.* **8**, 863–884. (doi:10.1002/2015MS000584)
28. Bacmeister JT, Wehner MF, Neale RB, Gettleman A, Hannay C, Lauritzen PH, Caron JM, Truesdale JE. 2014 Exploratory high-resolution climate simulations using the Community Atmosphere Model (CAM). *J. Clim.* **27**, 3073–3099. (doi:10.1175/JCLI-D-13-00387.1)
29. Wehner MF, Smith RL, Bala G, Duffy P. 2010 The effect of horizontal resolution on simulation of very extreme US precipitation events in a global atmosphere model. *Clim. Dyn.* **34**, 241–247. (doi:10.1007/s00382-009-0656-y)
30. Gent PR *et al.* 2011 The community climate system model version 4 (CCSM4). *J. Clim.* **24**, 4973–4991. (doi:10.1175/2011JCLI4083.1)
31. Collins WD *et al.* 2006 The community climate system model version 3 (CCSM3). *J. Clim.* **19**, 2122–2161. (doi:10.1175/JCLI13761.1)
32. Neale RB, Richter J, Park S, Lauritzen PH, Vavrus SJ, Rasch PJ, Zhang M. 2013 The mean climate of the community atmosphere model (CAM4) in forced SST and fully coupled experiments. *J. Clim.* **26**, 5150–5168. (doi:10.1175/JCLI-D-12-00236.1)
33. Lin SJ. 2004 A 'vertically Lagrangian' finite-volume dynamical core for global models. *Mon. Weather Rev.* **132**, 2293–2307. (doi:10.1175/1520-0493(2004)132<2293:AVLFDC>2.0.CO;2)
34. Yeager SG, Shields CA, Large WG, Hack JJ. 2006 The low resolution CCSM3. *J. Clim.* **19**, 2545–2566. (doi:10.1175/JCLI13744.1)
35. Kiehl JT, Shields CA. 2013 Sensitivity of the Palaeocene–Eocene Thermal Maximum climate to cloud properties. *Phil. Trans. R. Soc. A* **371**, 20130093. (doi:10.1098/rsta.2013.0093)
36. Joussame S, Braconnot P. 1997 Sensitivity of paleoclimate simulation results to season definitions. *J. Geophys. Res.* **102**, 1943–1956. (doi:10.1029/96JD01989)
37. Shields CA, Kiehl JT. 2016 Simulating the pineapple express in the half degree community climate system model, CCSM4. *Geophys. Res. Lett.* **43**, 7767–7773. (doi:10.1002/2016GL069476)
38. Shields CA, Kiehl JT. 2016 Atmospheric river landfall-latitude changes in future climate simulations. *Geophys. Res. Lett.* **43**, 8775–8782. (doi:10.1002/2016GL070470)
39. Braconnot P *et al.* 2007 Results of PMIP2 coupled simulations of the Mid-Holocene and Last Glacial Maximum—part 2: feedbacks with emphasis on the location of the ITCZ and mid- and high latitudes heat budget. *Clim. Past.* **3**, 279–296. (doi:10.5194/cp-3-279-2007)
40. Abels HA, Kraus MJ, Gingerich PD. 2013 Precession-scale cyclicity in the fluvial lower Eocene Willwood formation of the Bighorn Basin, Wyoming (USA). *Sedimentology* **60**, 1467–1483. (doi:10.1111/sed.12039)
41. Wing SL, Greenwood DR. 1993 Fossils and fossil climate: the case for equable continental interiors in the Eocene. *Phil Trans. Biol. Sci.* **341**, 243–252. (doi:10.1098/rstb.1993.0109)
42. Snell KE, Thrasher BL, Eiler JM, Koch PL, Sloan LC, Tabor NJ. 2013 Hot summers in the Bighorn Basin during the Paleogene. *Geology* **41**, 55–58. (doi:10.1130/G33567.1)
43. Lippert PC, Zachos JC. 2007 A biogenic origin for an anomalous fine-grained magnetic material at the Paleocene-Eocene boundary at Wilson Lake, New Jersey. *Paleoceanography* **22**, PA4104. (doi:10.1029/2007PA001471)
44. Stassen P, Thomas E, Speijer RP. 2012 Integrated stratigraphy of the Paleocene-Eocene Thermal Maximum in the New Jersey coastal plain: toward understanding the effects of global warming in a shelf environment. *Paleoceanography* **27**, PA4210. (doi:10.1029/2012PA002323)
45. Self-Trail JM *et al.* 2017 Shallow marine response to global climate change during the Paleocene-Eocene Thermal Maximum, Salisbury Embayment, USA. *Paleoceanography* **32**, 1–19. (doi:10.1002/2017PA003096)
46. Chen Z, Ding Z, Yang S, Zhang C, Wang X. 2016 Increased precipitation and weathering across the Paleocene-Eocene Thermal Maximum in central China. *Geochem. Geophys. Geosyst.* **17**, 2286–2297. (doi:10.1002/2016GC006333)
47. Pujalte V, Baceta JI, Schmitz B. 2015 A massive input of coarse-grained siliciclastics in the Pyrenean Basin during the PETM: the missing ingredient in a coeval abrupt change in hydrological regime. *Clim. Past.* **11**, 1653–1672. (doi:10.5194/co-11-1653-2015)
48. Solomon S, Qin D, Manning M, Chen Z, Marquis M, Averyt KM, Tignor M, Millier HL (eds). 2007 *Contributions of Working Group 1 to the Fourth Assessment Report of the Intergovernmental Panel on Climate Change*. Cambridge, UK: Cambridge University Press.